

# 3D z-Shim Method for Reduction of Susceptibility Effects in BOLD fMRI

Gary H. Glover\*

**Susceptibility-induced magnetic field gradients (SFGs) perpendicular to the slice plane often result in signal dropout in blood oxygenation level-dependent (BOLD) functional magnetic resonance imaging (fMRI) experiments. Two-dimensional (2D) z-shim methods reduce these effects by acquiring multiple images with different slice refocusing gradient areas. In this work a 3D z-shim method is introduced as a more efficient alternative. The technique augments the  $k$ -space data for a conventional 3D phase encoding acquisition with  $N$  additional lines that extend the  $k_z$  coverage sufficiently to sample  $k$ -space fully in regions with SFGs. Multiple subsets of these data are reconstructed using a sliding window that provides  $N + 1$  z-shim images. Fewer total acquisitions are required than with the 2D method for the same coverage, and finer z-shim steps are obtained. The technique is demonstrated with a motor task using intentionally introduced SFGs and compared with the 2D method. The results confirm increased BOLD SNR and activation with the new method in good agreement with theory. Magn Reson Med 42:290–299, 1999. © 1999 Wiley-Liss, Inc.**

**Key words:** functional magnetic resonance imaging; magnetic susceptibility effect; z-shim MR imaging

The most widely employed functional magnetic resonance imaging (fMRI) method uses blood oxygenation level-dependent (BOLD) contrast to depict neuronal activation (1). BOLD contrast derives from modulation of  $T_2^*$  by changes in the oxygen content of the microvasculature in cortex and surrounding tissues. Therefore, in sensitizing the nuclear magnetic resonance (NMR) signal to BOLD contrast using either a long-TE gradient-refocused echo (GRE) sequence or an asymmetric echo sequence (2), the technique is also made sensitive to other sources of  $T_2^*$ -induced signal losses. Such losses can occur in regions of the brain adjacent to air cavities where macroscopic magnetic field gradients are created, as in the frontal orbital or lateral temporal areas. The induced field heterogeneities can be severe enough to cause signal dropouts from intravoxel dephasing, which precludes acquisition of fMRI data in such regions (3). We term such macroscopic  $T_2^*$  effects morphology-induced intravoxel dephasing (MID), which derives from susceptibility-induced field gradients (SFGs).

An example is shown in Fig. 1, which displays  $T_2^*$ -weighted images (TE of 40 msec) obtained with a GRE spiral sequence at 1.5 T, and field maps that were generated

from two acquisitions with TEs of 6 and 8 msec. Also shown are plots of signal intensity,  $B(z)$  and  $dB/dz$  for three regions of interest (ROIs). Even though  $dB/dz$  is small compared with either slice-select or imaging gradient amplitudes, the long evolution time (TE) causes enough dephasing to result in nearly complete loss of signal in some regions of the most inferior slice.

In most fMRI techniques, the slice thickness is made larger than the in-plane resolution element size, as is the case here, so that the image voxels are highly asymmetric. With axial slices, therefore, MID effects are generated predominantly by gradients established along the largest voxel dimension, the slice ( $z$ ) direction.

Several methods have been proposed for mitigation of MID. One approach is the use of thinner slices (4) and higher resolution (5). However, the slice thickness must be made extremely small to compensate for MID, as we demonstrate in the next section. In addition, the signal-to-noise ratio (SNR) is compromised by acquiring thin slices and averaging to achieve the originally desired slice thickness. Furthermore, the spatial coverage and/or the temporal resolution is reduced, and therefore this method is not very efficient. Another approach uses tailored radiofrequency (RF) pulses to compensate for the gradients in the design of the pulse (6,7). The compensation works well in the MID neighborhood, but reduces signal elsewhere unless multidimensional excitation is employed (7).

A third approach to reduction of MID is the z-shimming method (3,8,9), whereby multiple ( $N_{zz}$ ) images are acquired with different z-direction phase-encoding values during each time frame, with the idea being that in different regions of the image with changing amounts of MID, different degrees of z-shim are necessary to provide local compensation. In practice this is accomplished by sequentially altering the area under the slice-encoding refocusing gradient lobe in a continuous cycle during acquisition of the time series, so that successive images have different amounts of z-shim. An output image is then calculated by complex summation (3), maximum-intensity projection (MIP), quadratic sum (9), or spatial domain mixing (9) over the  $N_{zz}$  images for each time frame. This method has been found to be highly effective in recovering signal in regions with severe signal loss. However, a penalty is paid in that for regions where no MID effects occur, little or no SNR advantage derives from the  $N_{zz}$  z-shim images, and in any case the temporal sampling is reduced by the factor  $N_{zz}$ . The desire for high temporal sampling constrains the number of z-shim images that can be acquired (typically  $N_{zz} = 3$  or 4), and this in turn may limit the effectiveness of the compensation.

In this work an alternative method is proposed, in which 3D acquisitions with extended  $k$ -space coverage in the  $z$  direction are employed to develop more efficiently a

Center for Advanced MR Technology at Stanford, Department of Diagnostic Radiology, Stanford University School of Medicine, Stanford, California.

Grant sponsor: NIH; Grant number: P41 RR 09784; Grant sponsors: the Lucas Foundation and GE Medical Systems.

The Center for Advanced MR Technology at Stanford is a program of the NIH National Center for Research Resources.

\*Correspondence to: Gary H. Glover, Lucas MRI Center, Department of Diagnostic Radiology, Stanford University School of Medicine, Stanford, CA 94305-5488. E-mail: gary@s-word.stanford.edu

Received 22 December 1998; revised 5 April 1999; accepted 7 April 1999.

© 1999 Wiley-Liss, Inc.

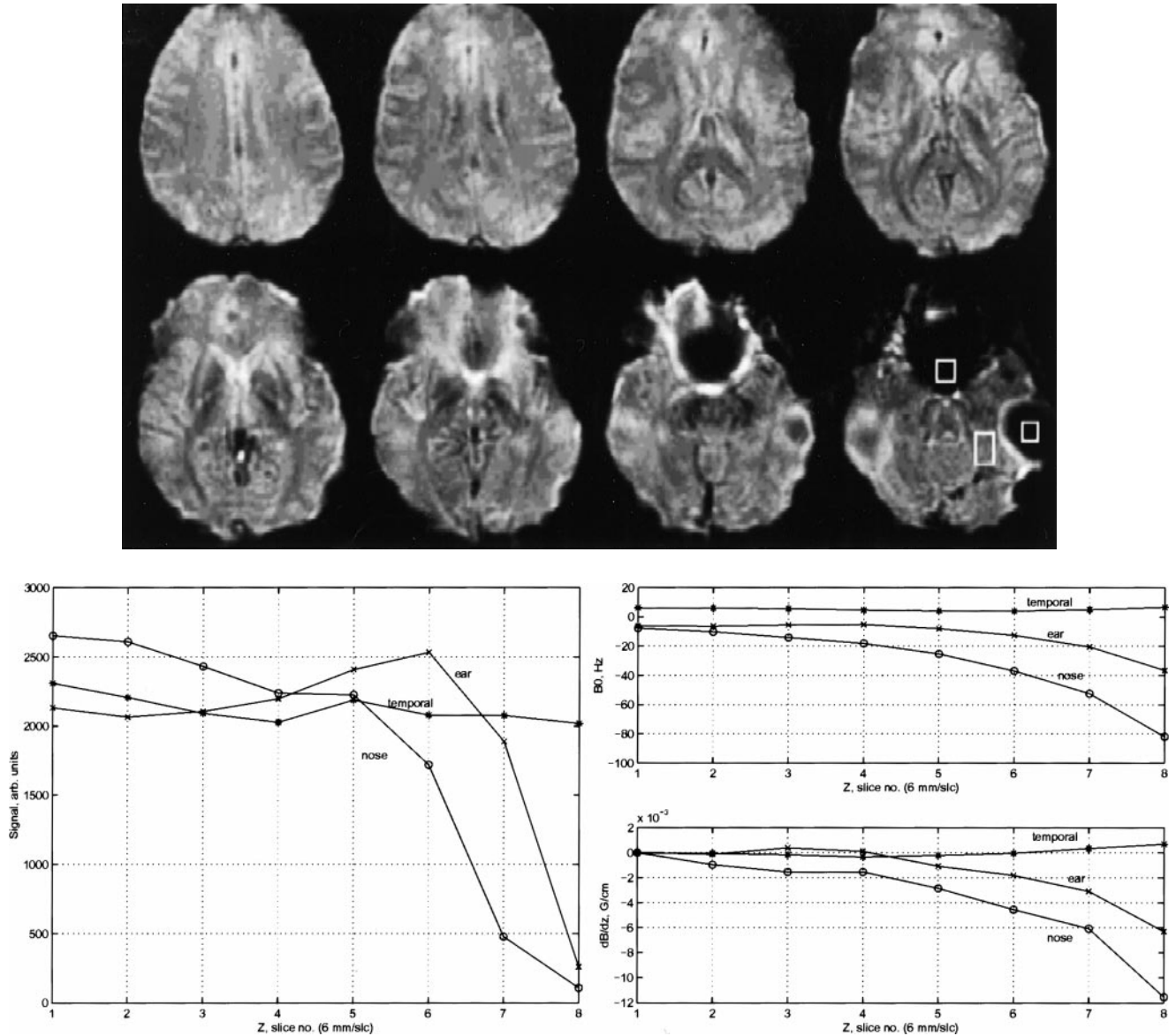


FIG. 1. Top:  $T_2^*$ -weighted 2D single-shot spiral images (TE 40 msec, slice thickness 6 mm, transverse resolution 2.2 mm, 1.5 T) showing signal loss due to susceptibility-induced field gradients (SFGs). Bottom: Plots of signal amplitude,  $B_0$  field, and  $dB/dz$  versus  $z$  (slice) in three regions outlined on slice 8 above. Gradients in the  $z$  direction exceeding 0.01 G/cm are sufficient to cause nearly complete loss of signal in the most inferior slice. Note that perturbation to field caused by nasal cavity creates effects that extend across the entire (48 mm) slab.

$z$ -shim data manifold with a larger effective  $N_z$  and higher SNR. The method demonstrated here uses a spiral trajectory in the  $x$ - $y$  direction and cartesian encoding in the  $z$  (slice)-encoding direction (“stack of spirals”) (4,10,11) because of the efficiency of spiral methods (11,12), but 3D echoplanar imaging [(EPI), or (EVI)] trajectories could also be employed (2). The method is first introduced and compared theoretically with the 2D  $z$ -shim method. Experiments are then described with passive imaging and with sensorimotor activation tasks in normal volunteers.

## THEORY

We first examine 2D  $z$ -shim methods, to develop the 3D  $z$ -shim method and compare the two approaches.

## 2D $z$ -Shim Method

During 2D slice selection, the applied slice-selection gradient causes phase encoding in the  $k_z$  (excitation) direction (13). The maximum extent in  $k_z$ -space covered by the slice-select gradient is

$$k_{max2} = \gamma G_s T_s = \omega_s T_s / W, \quad [1]$$

where  $\gamma$  is the gyromagnetic ratio,  $G_s$  and  $T_s$  are the amplitude and half-width of the slice-select gradient, respectively,  $W$  is the slice width, and  $\omega_s$  is the bandwidth of the radiofrequency (RF) pulse. For a pulse with 1.25 kHz bandwidth,  $T_s = 3.2$  msec and  $W = 5$  mm,  $G_s = 0.59$  G/cm, and  $k_{max2} = 8.0 \times (2\pi)$  cm<sup>-1</sup>. In regions where  $dB/dz = 0$ ,

the  $k_z$  trajectory is returned to the origin by the refocusing lobe and full signal results. However, for a brain region such as that depicted in Fig. 1 where SFGs occur in the slice direction, additional phase-encoding  $k_{\text{off}}$  occurs (8) during the entire TE period, and this unintended phase encoding leads to signal loss. If  $dB/dz$  can be approximated as a linear gradient across any one slice, the offset can be calculated as

$$k_{\text{off}} = \gamma G_z \text{TE}, \quad [2]$$

where  $G_z$  is the magnitude of the SFG. For an SFG having  $G_z = 0.01$  G/cm and  $\text{TE} = 40$  msec,  $k_{\text{off}} = 1.7 \times (2\pi) \text{ cm}^{-1}$ . When  $k_{\text{off}} \neq 0$ , the net transverse magnetization is reduced according to

$$M_t = M_o \text{sinc}(k_{\text{off}} W/2),$$

where for simplicity an ideal rectangular slice profile has been assumed, the spin density has been assumed uniform across the slice,  $M_o$  is the magnetization at the center of the slice, and  $\text{sinc}(x) = (\sin(x)/x)$ . With the parameters above, the fractional signal loss is  $M_t/M_o = 0.17$ . Thus even small gradients can lead to substantial signal losses.

With the 2D z-shim method,  $N_{a2}$  images are acquired with different phase encodings in the slice-select direction obtained by changing the area under the refocusing lobe,

$$k_{\text{shimi}} = f_i k_{\text{max}2}, 1 \leq i \leq N_{a2}, \quad [3]$$

with the expectation that the offset  $k_{\text{off}}$  for a given voxel is approximately compensated by one of the  $N_{a2}$  values of  $k_{\text{shimi}}$ . For the example given, the area of the refocusing lobe would need to be increased by a factor of about 1.2 for compensation. In the 2D case, the number of z-shim images  $N_{z2}$  that are used in generating the final z-shim image is equal to the number acquired,  $N_{a2}$ .

### 3D Acquisition

In the usual 3D acquisition with  $N_{\text{sl}}$  slices of width  $W$  each, phase encoding is applied in the  $k_z$  direction to span  $k_z \leq k_{\text{max}3}$ , where  $k_{\text{max}3} = \pi/W$  (Fig. 2). The increment between phase-encoding steps is

$$\Delta k_z = 2\pi/(N_{\text{sl}} W). \quad [4]$$

For  $W = 5$  mm,  $k_{\text{max}3} = 2\pi \text{ cm}^{-1}$ , and thus for the example given the SFG shifts the  $k$ -space origin enough that it lies outside the range of the 3D  $k_z$  encoding ( $k_{\text{off}} > k_{\text{max}3}$ ), as shown in Fig. 2a. However, in general most of the image spectral density lies at the  $k$ -space origin. Therefore, the 3D acquisition results in greater loss of signal than for the 2D case for equal slice thickness. Note that with the slice thickness decreased to 2.5 mm, however,  $k_{\text{max}3}$  is doubled so that the  $k_z$ -space origin is sampled ( $k_{\text{max}3} = 4\pi > k_{\text{off}}$ ), and the MID effect is decreased (Fig. 2b). In this case, twice as many slices would be needed to cover the same volume.

One way to reduce MID, therefore, is to use 3D acquisitions with thin slices and average the acquired slices to

achieve the desired  $W$ , as described by Lai (4). The penalties are that the time/frame is increased and the SNR outside the MID region is reduced. If the 3D acquisition uses a repetition time  $\text{TR}_3 = \text{TR}_2/N_{\text{sl}}$ , where  $\text{TR}_2$  is the corresponding time for the 2D case,  $N_{\text{sl}}$  3D  $k_z$ -space samples will require the same time to acquire as one time frame of  $N_{\text{sl}}$  slices using a 2D sequence. Doubling  $N_{\text{sl}}$  will therefore double the time/frame. Like the 2D z-shim method, this approach is therefore not efficient.

### 3D z-Shim Method

In the proposed 3D z-shim method it is recognized that additional coverage in  $k_z$ -space is needed in order that  $k_{\text{off}}$  lie within the sampled space, but that in many cases the  $k_{\text{off}}$  for all voxels of interest is unipolar (e.g., Fig. 1), because the air cavities that generate the SFGs are predominantly superior or inferior to the volume of interest. With this assumption there is no need to increase the  $k_z$  span symmetrically, as occurs with the use of thinner slice 3D. It is only necessary to add samples on one side of the origin (with the same spacing  $\Delta k_z$  given in Eq. [4] to ensure that a full sampling is achieved. The new maximum  $k$ -space sampling extent required is

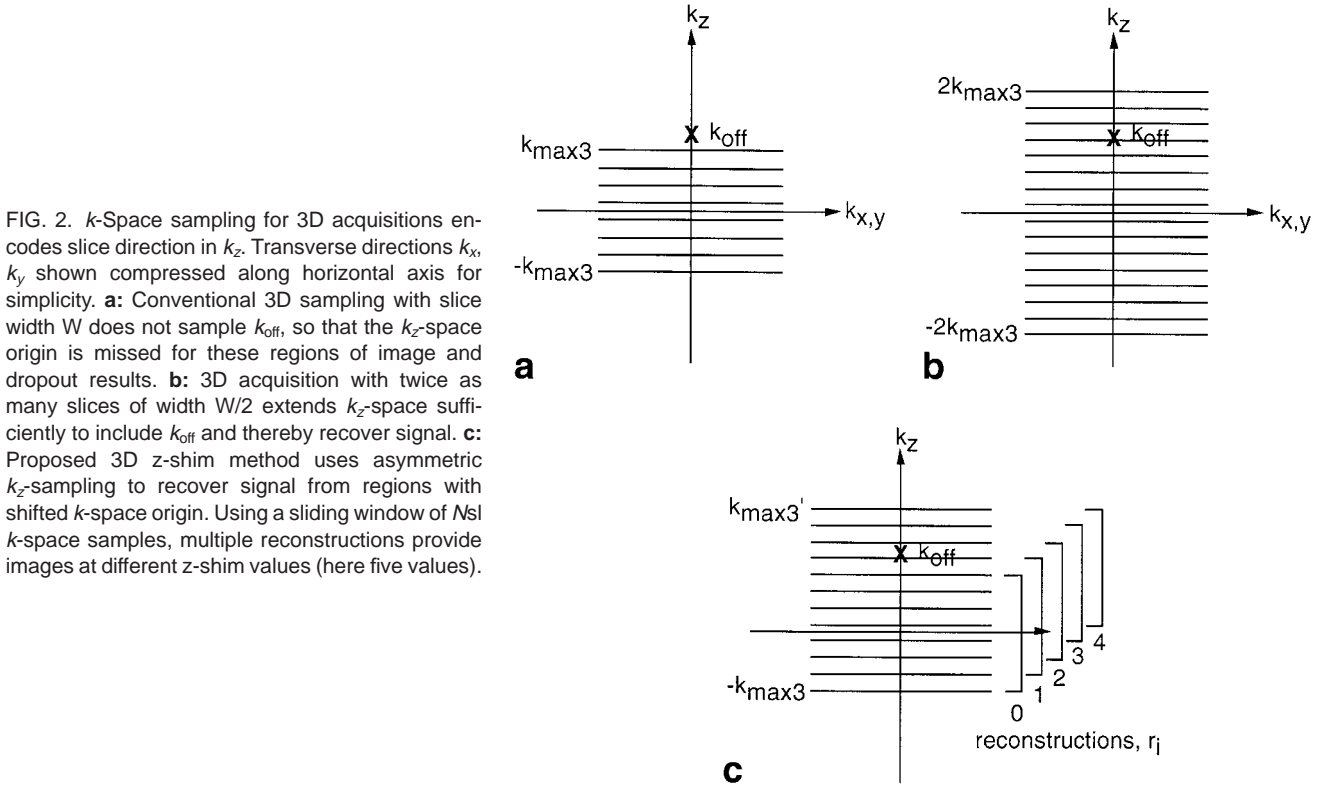
$$k_{\text{max}3'} = k_{\text{max}3} + |k_{\text{off}}|, \quad [5]$$

where  $k_{\text{off}}$  is for the worst-case voxel. This situation is shown in Fig. 2c. A sliding  $N_{\text{sl}}$  subset of the collected samples is used to reconstruct  $N_{\text{sl}}$  slices with thickness  $W$  having full  $k$ -space coverage,  $k_z \leq k_{\text{max}3}'$ . The total number of  $k$ -space samples needed is  $N_{k3}$ , given by

$$N_{k3} = N_{\text{sl}} + |k_{\text{off}}|/\Delta k_z = N_{\text{sl}} (1 + k_{\text{off}} W/2\pi). \quad [6]$$

Thus a factor  $N_{a3}$  ( $N_{k3}/N_{\text{sl}}$  acquisitions are gathered with respect to the no-z-shim case, from which  $N_{z3} = N_{k3} - N_{\text{sl}} + 1$  3D z-shim images can be reconstructed. With the example given,  $N_{k3} = 1.85 N_{\text{sl}}$ . If  $N_{\text{sl}} = 8$  images, this means 7 3D z-shim images are obtained for an acquisition time increased by a factor of  $\sim 1.85$ . By comparison, with the 2D z-shim method the scan time/frame increases by the factor  $N_{a2} = N_{z2}$  ( $= 3$  or  $4$ ), just the number of z-shim images. Thus, the 3D method makes more efficient use of the acquisition time.

In practice, the algorithm is applied by reconstructing  $N_{z3}$  full 3D image sets using a sliding window of  $N_{\text{sl}}$  contiguous  $k_z$  samples, as shown in Fig. 2c. In this way, finer steps between z-shim values are provided than with the 2D z-shim method. From these z-shim image sets a single output image is generated. For each output voxel, the proper choice among the  $N_{z3}$  input voxels can be made by several means. First, if a  $B_0$  field map is available  $k_{\text{off}}$  can be calculated using Eq. [1] for each voxel and used to choose directly the corresponding reconstruction that matches  $k_{\text{off}}$ . Second, the proper choice will correspond to maximum signal, and thus a MIP or sum of squares combination can also be employed (9). In any case, only 1 or  $\sim 1$  image is used in the output image as in 2D z-shimming, and therefore an SNR penalty will result be-



cause only  $Nsl$  samples contribute to the image while  $N_{a3}$  samples are acquired. Accordingly, we next examine the SNR for 2D and 3D methods.

#### Signal-to-Noise Ratio

To compare the 2D and 3D methods, assume that scan time  $T$ , slice thickness  $W$ , and number of slices  $Nsl$  are the same for both methods. It is further assumed that a common single-shot method (e.g., spiral) is used for the 2D and  $k_x$ - $k_y$  dimensions of the 3D method and that the Ernst angle is chosen for each TR. The number of time frames that can be acquired for the 2D case with repetition time  $TR_2$  is

$$Nf_2 = (T/TR_2)/N_{a2}. \quad [7]$$

The SNR for the entire 2D z-shim scan is then ( $Nf_2$  times that of one time frame, and is given by

$$SNR_2 = \left( \frac{Nf_2}{\sigma_o^2} \frac{1 - E_2}{1 + E_2} \right)^{1/2}, \quad [8]$$

where  $\sigma_o$  is the noise and  $E_2$  ( $\exp(-TR_2/T_1)$ ), with  $T_1$  the longitudinal relaxation time. For the 3D case, there are  $Nf_3$  time frames, where

$$Nf_3 = (T/TR_3)/N_{k3} = (T/TR_2)/N_{a3}. \quad [9]$$

Then, the SNR for the 3D scan is given by

$$SNR_3 = \left( Nf_3 \frac{Nsl}{\sigma_o^2} \frac{1 - E_3}{1 + E_3} \right)^{1/2}, \quad [10]$$

where  $E_3 = \exp[-TR_2/(Nsl T_1)]$ . From Eqs. [9] and [10], the ratio  $R$  ( $SNR_3/SNR_2$ ) is given by

$$R = \left\{ Nsl \frac{1 - E_3}{1 + E_3} \frac{1 + E_2}{1 - E_2} \right\}^{1/2} \left( \frac{N_{a2}}{N_{a3}} \right)^{1/2} = R_o \left( \frac{N_{a2}}{N_{a3}} \right)^{1/2}, \quad [11]$$

with

$$R_o \equiv \left\{ Nsl \frac{1 - E_3}{1 + E_3} \frac{1 + E_2}{1 - E_2} \right\}^{1/2} \approx \left[ \frac{TR_2}{2 T_1} \frac{1 + E_2}{1 - E_2} \right]^{1/2}, \quad [12]$$

where the approximation holds if  $TR_2 \ll Nsl T_1$ . The term  $R_o$  represents the ratio of SNRs for conventional (non-z-shim) 3D and 2D techniques. With  $TR_2 = 1400$  msec,  $T_1 = 800$  msec,  $N_{z2} = 3$ ,  $Nsl = 8$ , and other parameters from the example,  $R = 1.4$  and  $R_o = 1.1$ . The ratio  $R/R_o$  ( $= 1.27$ ) represents the benefit of the 3D z-shim method that results from acquiring less data/output frame.

## MATERIALS AND METHODS

The 2D z-shim and new 3D z-shim methods were compared by performing static acquisitions as well as finger tapping experiments on three normal right-handed subjects (two men and one woman). In the static experiments, 2D and 3D z-shim scans were obtained in axial orientation to cover a range of the brain where MID occurred, while the subjects lay passively. The purpose of these experiments was to explore parameters and demonstrate qualitatively the effectiveness of the z-shim methods in various brain regions. For the finger tapping experiments, intentional

SFGs that encompassed the sensorimotor cortex in one hemisphere were introduced by placing a small (29.3 mm diameter) bottle of gadolinium (Gd)-doped water near the head. It was found that the bottle introduced SFGs with a significant component in the z direction that was unipolar across the sensorimotor cortex. Scans were obtained with each z-shim method with and without the bottle, and the degree of recovery of signal from the introduced susceptibility perturbation was quantitated. In addition, the SNR was compared from the activation Z scores in sensorimotor cortex.

#### Data Acquisition

All experimental data were obtained with a 1.5 T scanner equipped with high-performance gradients and receiver (GE Signa Echospeed, rev 5.7, Milwaukee, WI).  $T_1$ -weighted fast spin-echo (FSE) scans were acquired for anatomic reference (TR/TE of 68/3000 msec, echo train length 8). Static and functional acquisitions used 2D (14) and 3D (4) spiral gradient-recalled echo sequences with a TE of 40 msec and a field of view of 20 cm. The in-plane trajectory was a single-shot, 40 msec duration uniform density spiral common to both pulse sequences, providing resolution of 2.2 mm (matrix  $90 \times 90$ ). Sixteen contiguous 5 mm thick axial slices were acquired for the static scans, while eight slices were obtained during the activation experiments. Acquisition parameters for all experiments are summarized in Table 1. A small, receive-only elliptical birdcage head coil was used for all scans (15), and subjects were stabilized with foam padding packed tightly in the coil. Images were reconstructed into a  $128 \times 128$  matrix with an off-line computer (Sun Microsystems, Mountain View, CA) using gridding and fast Fourier transforms (FFTs). Linear shim corrections for each slice were applied during reconstruction (14).

The 2D sequence employed a sinc slice-select RF pulse with phase duration  $8\pi$  (6.4 msec) having a bandwidth of 1.25 kHz. This pulse allowed the use of contiguous slice spacing with minimal signal loss. z-Shimming was performed by altering the area of the slice-selection refocusing pulse in a sequential order. During the passive scans  $f_i$  was varied over the range  $0.6 \leq f_i \leq 1.0$ . It was determined that only a subset need be covered for the areas of interest, and subsequent activation experiments used  $N_{z2} = 3$  and  $f_i = (1.0, 0.9, 0.8)$ . The  $f_i$  value was held constant while all slices were obtained. Thus for the activation experiments three TR periods were required in order to obtain all slices with the three values of z-shim. A total of 144 time frames

(48 z-shimmed time frames) was acquired with a scan duration of 201.6 sec.

The 3D sequence used a TR of 175 msec and a flip angle of  $30^\circ$ , thereby employing the same data collection rate as for the 2D scans (i.e., 1400 msec was required for a conventional 8-slice 3D acquisition). During the static experiments 16 slices with 16 additional  $k_z$  phase encodings were acquired, while the activation experiments acquired 8 slices and 6 additional  $k_z$  phase encodings to augment the 8 conventional  $k_z$  lines. For the latter, a total of 82 time frames (each with  $N_{k3} = 14$   $k_z$  encodings) was acquired for a scan time of 200.9 sec. From each frame, 7 z-shimmed image volumes of 8 slices each with 5 mm slice thickness were reconstructed using the sliding "boxcar" window arrangement in Fig. 2c with  $N_{sl} = 8$  encodings for each reconstruction.

#### Activation Scan Technique

Bilateral sequential finger apposition was performed by the volunteers at a controlled 3 Hz rate, to reduce unintended variations in activation (16,17). Auditory cueing tones were generated by a custom program on a Macintosh computer (Mountain View, CA) and delivered by pneumatic earphones (Resonance Technology, Van Nuys, CA).

A block-trial paradigm was used with five cycles of 20 sec on/ 20 sec off for a total duration of 200 sec for each scan. The 2D activation scan was first obtained. The bottle of doped water was then placed adjacent to the left side of the head, and short acquisitions with the 2D technique were used to adjust the position of the bottle so that a signal loss was introduced in the area of the central sulcus. A second 2D activation scan was then obtained, followed by the 3D acquisition. The bottle was then removed and a final 3D activation scan acquired.

#### Image Analysis

##### *z-Shim Image Construction*

For each slice and time frame,  $N_{z2} = 3$  images were available in the 2D case and  $N_{z3} = 7$  images in the 3D case with different values of z-shim. Output z-shimmed time frames were created by a simple MIP operation through the z-shim component images (48 2D z-shim images, 82 3D z-shim images). In addition to the z-shimmed images, uncorrected images were also obtained from the same data sets (the  $f = 0$  image in the 2D case, and the  $k_{off} = 0$  image in the 3D case).

#### Activation Analysis

Activation maps were generated using cross-correlation of the final z-shimmed images with a sine wave after linear trend removal (18,19), and the resulting maps were overlaid on the  $T_1$ -weighted scans. The Z scores were calculated by Fisher transformation taking into account temporal autocorrelation (20). Volumes of activation were calculated by fitting a normal distribution to the histogram of Z scores and subtracting the normally distributed background fit from the measured histogram (21). The number of activated voxels was defined as the area under the difference distribution having Z scores  $\geq 2.0$ . The effects of gross motion and vessels were eliminated by requiring that

Table 1  
Scan Parameters

	2D		3D	
	Static	Activation	Static	Activation
Nslice	16	8	16	8
Nframes	5	144	2	82
TR (msec)	2800	1400	175	175
T (sec)	14.0	201.6	5.6	200.9
Flip angle ( $^\circ$ )	90	80	30	30
$N_{z2,3}$	5	3	17	7
$f_i$	0.6–1.0	0.8–1.0	—	—
$N_{k3}$	—	—	32	14

the time series standard deviation after removal of the activation component was  $\leq 0.5\%$  of the mean image intensity for each activated voxel. The activation volume and average Z scores for each subject were tabulated by summing across all slices for which insertion of the doped bottle caused loss of activation. Separate values were maintained for left and right hemispheres, and the supplementary motor area (SMA) was excluded from the volumes. The right hemisphere thereby served as a control between scans with bottle present and absent. The volumes were compared by normalizing with the number of activated voxels for the scans with bottle absent to control for differences in subjects and number of slices.

The analysis was performed using z-shimmed as well as uncorrected images for the scan in which the doped bottle was introduced, and was performed using the uncorrected images for the uncorrupted scans. In this way, the effect of the z-shim corrections on the induced “hole” could be observed and the degree of recovery of the BOLD signal determined. The six sets of activation maps for each subject and the group averages were compared using paired *t*-tests.

## RESULTS

### Static Scans

Figure 3 illustrates the 3D technique and compares results with those from the 2D method using non-activation scans for one volunteer, but similar results were obtained for other subjects. Both 2D and 3D sequences were able to reduce the MID artifacts substantially. In the 3D case, 16 additional *k*-space offset values were acquired (Fig. 3a), thereby allowing 17 z-shim images to be reconstructed in a scan time of 5.6 sec/volume, with finer steps than in the 2D acquisition. In the 2D case, only three images with  $f \geq 0.8$  (Fig. 3c) contributed to the MIP, and the scan time/volume for three images is 8.4 sec, although five steps were actually acquired. Note that in uniform regions of the brain, little change in the 3D z-shim component images occurs as the offset is increased until the offset becomes  $N_{sl}/2$  (first seven images in Fig. 3a), at which point the center of *k*-space for those regions is no longer sampled. In the nasal cavity region, the required offset for peak signal (i.e., to cover the *kz*-space origin) is substantial and not reached in the three-step 2D acquisition.

The 3D results show improved fill-in of the MID regions over the 2D method, although some ringing near the edges of the frontal MID region is apparent. The ringing is the result of off-resonance effects in the spiral trajectory. This could be reduced with a shorter acquisition window during the spiral readout, but an intentionally long duration (40 msec) readout was chosen as a worst case. These effects are static and do not significantly affect the time series.

### Activation Scans

Figure 4 shows the component and z-shim (MIP) images for one subject as well as the corresponding activation maps. The 2D and 3D z-shim sequences provided similar compensation for the susceptibility “hole” introduced by the bottle, but the 3D sequence acquired a greater number of

time frames (82 vs. 48) because fewer total acquisitions/frame were required. This resulted in greater activated volumes for the 3D z-shim method in both the right hemisphere (control) brain region and the left hemisphere, as shown in Fig. 4c and d

The results of quantitating the activation volumes and average Z scores in the activated volumes are shown in Table 2. The data were averaged across subjects and are summarized in Fig. 5. The results for the right, control hemisphere were pooled across scans because there was no significant difference between scans without and with the bottle present. In the left hemisphere, the 3D z-shim method provided significantly greater activation volumes than the 2D method, even though the starting volumes with the bottle present were not different (Fig. 5a). The activation volumes in the control hemisphere were significantly larger for the 3D scan. The average Z scores were greater for the 3D scans, as shown in Fig. 5b, and those differences were significant in the control hemisphere as well as for the left hemisphere without the bottle present and with the z-shimmed condition. The Z scores for the 2D scans did not differ between unperturbed, uncorrected or corrected scans. The scores for the 3D z-shim method were significantly higher than those for the uncorrected 3D scans, however.

## DISCUSSION

SFGs can be severe enough to cause signal dropouts in BOLD fMRI. Often the SFGs are predominately perpendicular to the slice plane and cause loss of signal because the added phase encoding in the *kz* direction is not compensated for by the slice-selection refocusing gradient. Previously it has been shown that 2D z-shim methods can reduce these signal losses by altering the refocusing gradient area in several steps. However, the recovery of signal in MID regions often comes at the expense of diminished efficiency in other, uniform regions of the brain. In many cases this is a handicap because activation may occur in multiple cortical regions that include both uniform and non-uniform magnetic field distributions. The penalty is a function of the number of z-shim images since only one of the component images contributes significantly to the final corrected image when MIP or comparable processing is used. The final statistical map is thereby penalized by approximately the square root of the same factor in uniform regions.

The process of altering the slice refocusing gradient area is equivalent to the *kz* phase-encoding step in a 3D acquisition. However,  $k_{max}$  for a conventional 3D scan is less than the equivalent encoding in 2D slice selection for the same slice thickness, and therefore conventional 3D scans are more prone to susceptibility losses than the 2D counterpart, as shown in Figs. 3a and c or 4a and b. One approach to reducing this loss in a 3D acquisition is to decrease the slice thickness, i.e., to increase  $k_{max}$ . This leads to loss of SNR and is therefore inefficient.

The 3D z-shim method extends the *kz* phase encoding in a fashion similar to increasing the slice resolution, but only does so in the direction needed to encompass the offset  $k_{off}$  in MID regions of interest. A sliding subset of the acquired *kz* lines is then reconstructed for various shifts of the center, as in Fig. 2c, which provides the same slice

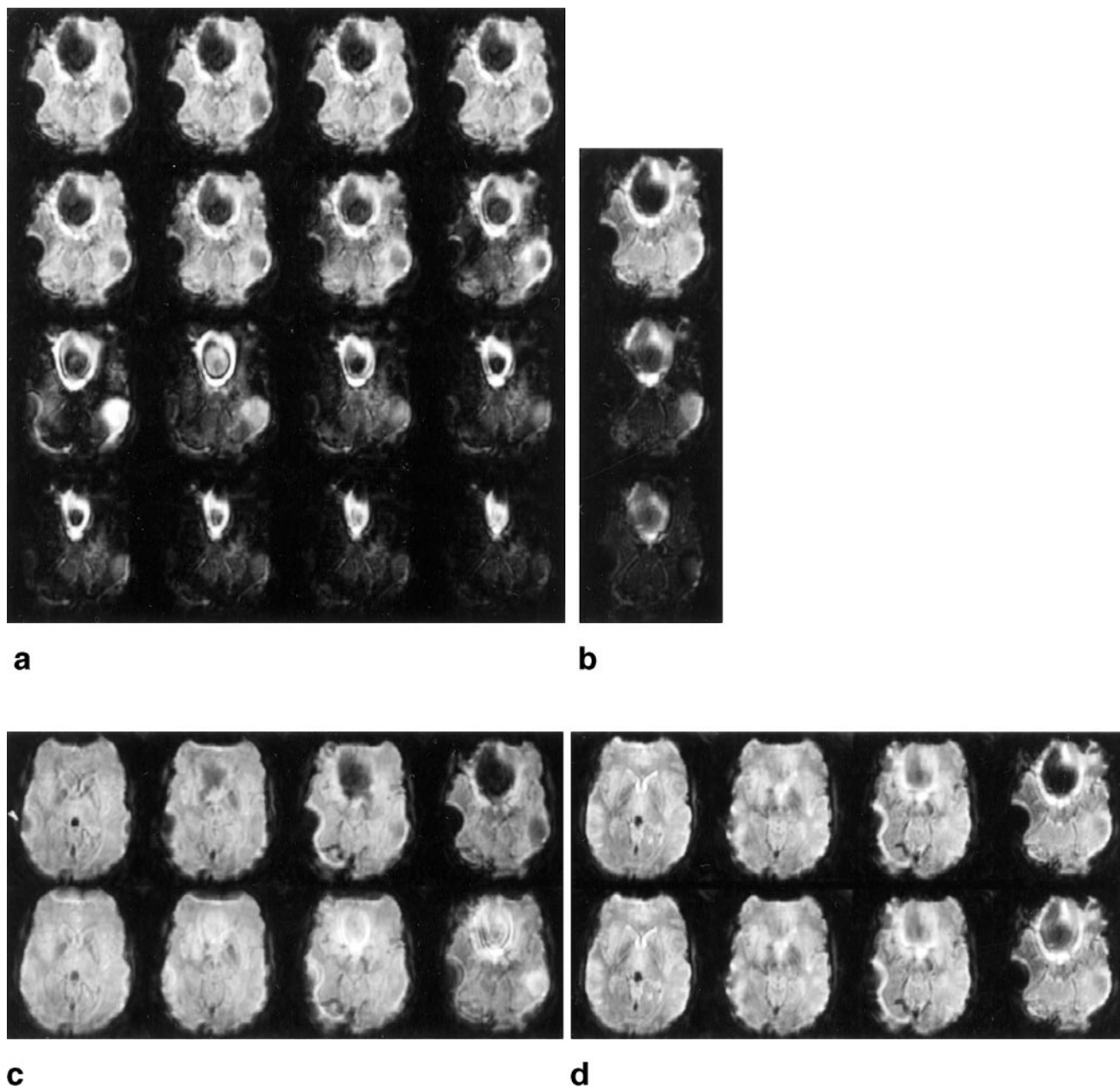


FIG. 3. Static images illustrating 3D z-shim technique (a,b) and comparing with 2D technique (c,d). **a:** 3D component images (first 16 of 17) for one of 16 slices. **b:** 3D uncompensated images (top) and resulting z-shimmed images (bottom) obtained by MIP through component images, for 4 of 16 slices. **c:** 2D component images for same slice as a. **d:** 2D uncompensated images (top) and resulting z-shimmed images (bottom) obtained by MIP through component images. Comparing b with d, the 3D method affords superior compensation in the nasal regions despite decreased scan time (5.6s vs. 8.4 sec per volume), because 3D component images extend further in z-shim space (cf. a and c).

thickness and SNR as the conventional scan. The number of additional lines needed to cover the  $k_{\text{off}}$  is thereby smaller than the factor needed for 2D z-shim. The economy is realized because  $kz$ -lines are shared between reconstructed z-shim component images, as demonstrated in Figs. 3b and 4b. Because the step size  $\Delta k_z$  in phase encoding is finer than can be employed in the 2D z-shim method due to scan time constraints, a larger number of 3D z-shim component images are generated. However, approximately  $N_{\text{sl}}/2$  of these images are roughly equivalent in uniform regions because the  $kz$ -space origin remains included as the subset shifts.

The quantitation of activation volumes and Z scores shows that the 3D method generally provides increased activation due to the more efficient utilization of the scan time, as shown graphically in Fig. 4d. From Table 2 and Fig. 5, the normalized activation volumes for the 3D method was significantly greater than for the 2D method,  $1.13 \pm 0.30$  vs.  $0.88 \pm 0.21$  in the left hemisphere with the bottle inserted ( $P = 0.05$ ), and  $1.31 \pm 0.27$  vs.  $0.94 \pm 0.04$  in the right hemisphere pooled across bottle/no-bottle experiments ( $P < 0.001$ ). There was no difference between the activation volumes in the left hemisphere without the z-shim correction for either 2D or 3D scans. The fractional

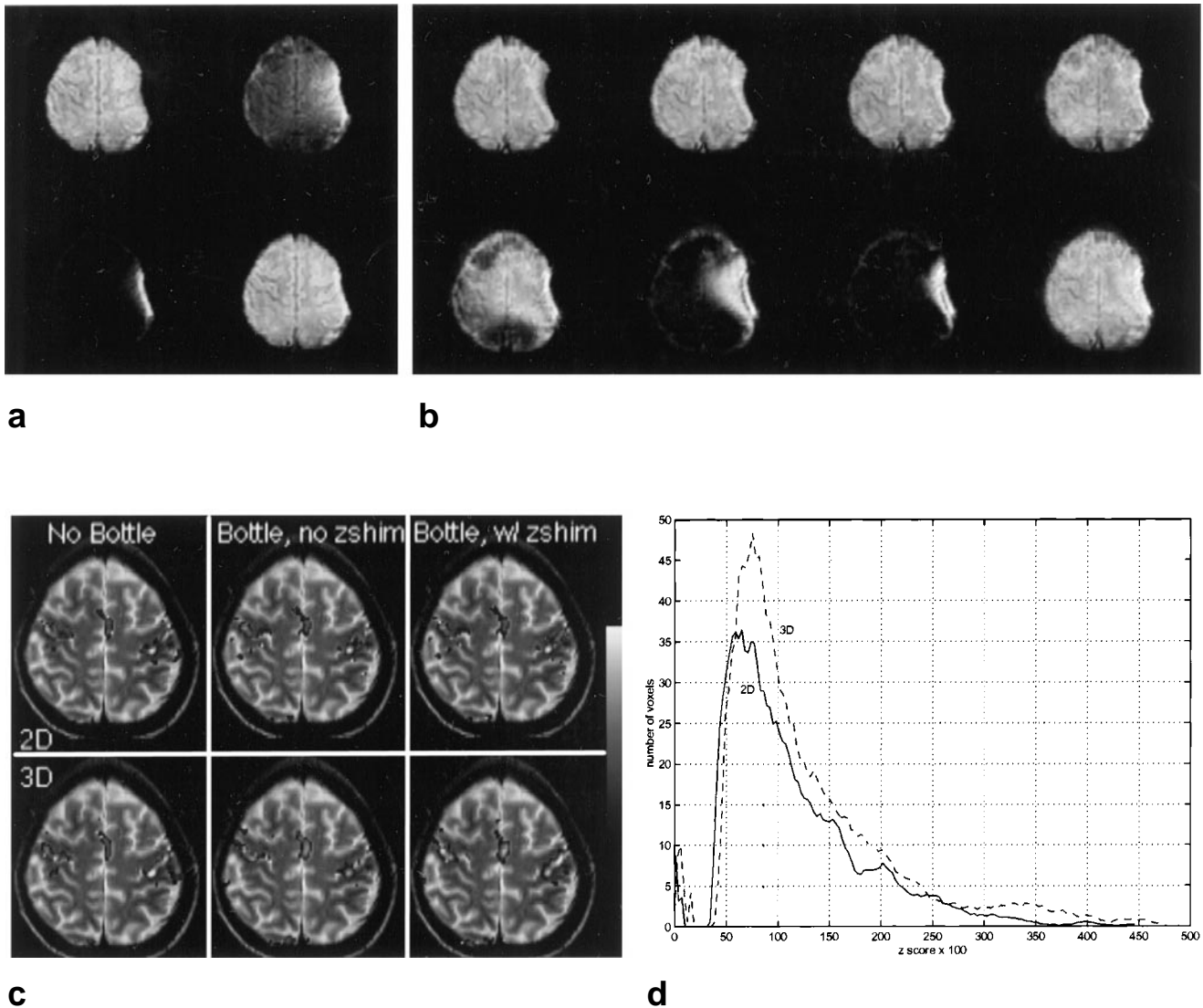


FIG. 4. Activation scans for one slice of subject 1. **a**: Three 2D z-shim component images and resulting z-shimmed image obtained by MIP. **b**: Seven 3D z-shim component images and resulting z-shimmed image. **c**: Activation maps comparing 2D (top row) and 3D (bottom row) z-shim methods. **d**: Histograms of activated voxels confirming increased volume for 3D method.

increase in activation volume for the 3D method was 1.28 in the left hemisphere and 1.39 in the right hemisphere, in good agreement with the factor of 1.27 predicted from Eq. [12].

The increase in average Z scores in the right hemisphere (opposite to the bottle insertion location) was smaller than the volume increase ( $2.97/2.67 = 1.11$ ). This results because the activated pixels do not benefit fully from the increased sampling (number of time frames) afforded by the higher efficiency 3D method, because the autocorrelation width from hemodynamic filtering is wider than the sampling interval and the full ( $N_f$ ) advantage is not realized. In non-activated pixels without temporal filtering, however, the background false positives are suppressed with the full ( $N_f$ ) averaging. This leads to the greater activation volumes from improved contrast.

The post-processing step employed in this work used simple projection (MIP) through the z-shim component images. A more exact approach would be to use the  $B_0$  map to calculate  $k_{\text{off}}$  (Eq. [2]), and choose the appropriate z-shim

component image for each voxel. However, other combination methods may be able to take greater advantage of the increased sampling for uniform-field brain regions, using the largely redundant reconstructions for the first few  $kz$  offsets (e.g., the first four images in Fig. 4b). Averaging these images instead of choosing between them would provide additional SNR ( $\sim(16/13 = 1.1$  here), since one independently measured  $kz$  line is introduced with each adjacent image. Of course, some blurring of these images occurs in the slice direction as the origin is shifted, since this operation amounts to partial  $k$ -space reconstruction without correction for the missing high frequencies on one side of the origin. This will reduce the advantage of this type of processing.

As presented here, the z-shim methods (both 2D and 3D) do not compensate for SFGs in directions other than the slice/slab select direction. These methods are nevertheless effective, however, because with axial scan plane orientation, the z direction is likely to be the most troublesome one since the slice thickness is generally larger than the

Table 2  
Activation Results

Subject no.	Left hemisphere (bottle side) (No. of pixels/ average Z score)		Right hemisphere (control) (No. of pixels/ average Z score)	
	2D	3D	2D	3D
	1			
No bottle	81/2.70	101/3.06	101/2.76	73/3.32
With bottle				
No z-shim	45/2.90	57/2.83	89/2.71	112/3.18
z-shim	58/2.81	87/3.12	90/2.70	111/3.10
2				
No bottle	158/2.63	150/2.90	89/2.47	105/2.86
With bottle				
No z-shim	136/2.73	103/2.84	86/2.63	105/2.84
z-shim	178/2.81	219/3.03	86/2.63	98/2.74
3				
No bottle	107/2.59	153/2.71	92/2.70	122/2.74
With bottle				
No z-shim	76/2.64	123/2.79	87/2.70	175/2.99
z-shim	88/2.65	164/2.82	88/2.72	180/2.93
Average no. of activated pixels, normal- ized with no-bottle data				
With bottle				
No z-shim	0.71 ± 0.13	0.68 ± 0.12	0.93 ± 0.05	1.26 ± 0.37
z-shim	0.88 ± 0.21	1.13 ± 0.30	0.94 ± 0.04	1.31 ± 0.33

in-plane resolution and the anatomy tends to induce gradients along the superior-inferior direction with superconducting solenoidal magnets.

The new 3D method was demonstrated with the simplifying assumption that the induced gradients are unipolar. This is certainly not a good assumption in general, especially when volume coverage includes regions near the base of the brain as well as near the sphenoid sinus. However, the technique does not depend on the unipolarity assumption and can easily be extended to compensate for SFGs of both polarities. The 3D method will remain more efficient than the 2D technique when bipolar z-shimming is required, since both techniques are penalized, and the same or greater view-sharing economies will be realized with the 3D method.

In addition, the 3D z-shim method could be extended to correct SFGs in the  $x$  and  $y$  directions by overscanning  $k$ -space in the appropriate directions and reconstructing subsets of the 3D cartesian space, in exactly the same fashion as demonstrated here in the  $kz$  direction, and with similar economies over the "brute force" method of increasing the in-plane resolution. An EPI trajectory might prove more effective than an elliptical spiral trajectory (22) for this application.

In conclusion, 3D z-shim methods may have significant advantages over 2D methods because of increased efficiency in the use of acquisition time. The advantages are manifested as increases in activation volume and Z scores. While the technique was demonstrated with a "stack of spirals" trajectory, EVI methods could also be employed.

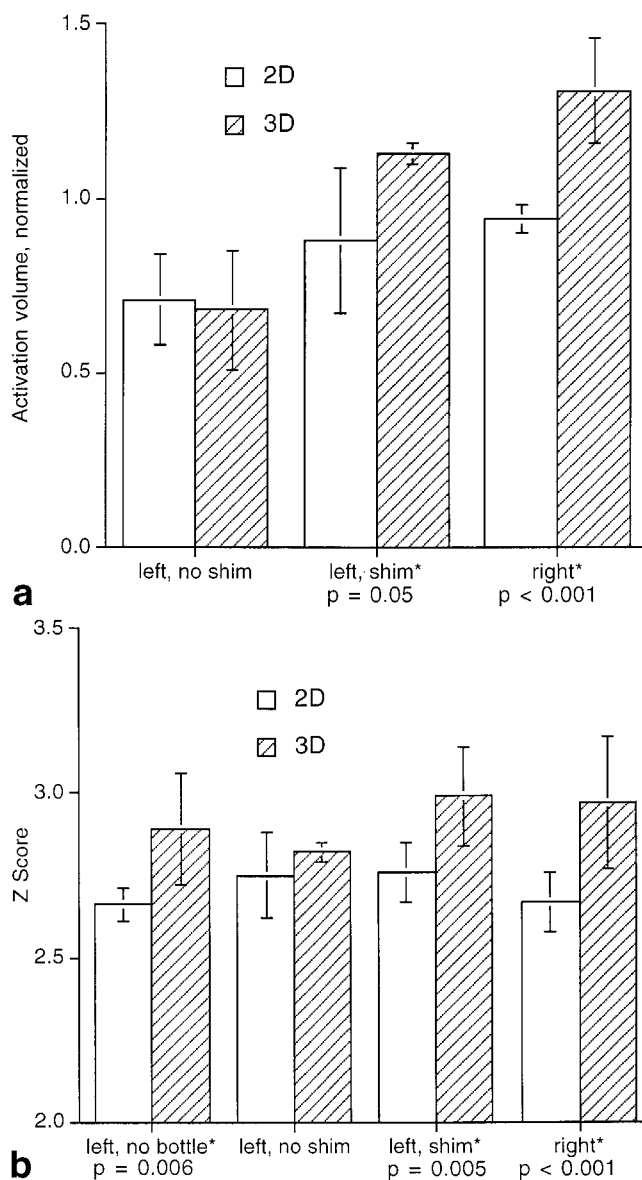


FIG. 5. Summary of averaged activation results (mean  $\pm$  SD) comparing 2D and 3D z-shim methods. Statistically significant differences between 2D and 3D results are marked with \* and  $P$  values for one-tailed  $t$ -test are given. **a**: Normalized activation volumes, without and with z-shim corrections, with bottle in place. Data for right hemisphere (control) are pooled. In addition to the 2D/3D differences noted on the plots, the differences between left-hemisphere activation volumes without and with z-shim were significant for both the 2D and 3D scans ( $P = 0.04$  and  $0.001$ , respectively). **b**: Average Z scores comparing scans without bottle to scans with bottle in place and without and with z-shim. In the left hemisphere, the 2D z-shim did not significantly alter the Z scores, but the scores were significantly increased for the 3D z-shim correction ( $P = 0.01$ ). In general, 3D scans have greater activation volumes and Z scores than corresponding 2D scans.

#### ACKNOWLEDGMENTS

The author is indebted to Jeff Duyn for beneficial discussions and A.M. Sawyer-Glover for assistance with scanning.

## REFERENCES

- Ogawa S, Tank DW, Menon R, Ellermann JM, Kim SG, Merkle H, Ugurbil K. Intrinsic signal changes accompanying sensory stimulation: functional brain mapping with magnetic resonance imaging. *Proc Natl Acad Sci USA* 1992;89:5951–5955.
- Yang Y, Mattay VS, Weinberger DR, Frank JA, Duyn JH. Localized echo-volume imaging methods for functional MRI. *J Magn Reson Imaging* 1997;7:371–375.
- Yang QX, Williams GD, Demeure RJ, Mosher TJ, Smith MB. Removal of local field gradient artifacts in  $T_2^*$ -weighted images at high fields by gradient-echo slice excitation profile imaging. *Magn Reson Med* 1998;39:402–409.
- Lai S, Glover G. Three-dimensional spiral fMRI technique: a comparison with 2D spiral acquisition. *Magn Reson Med* 1998;39:68–78.
- Haacke EM, Hopkins A, Lai S, Buckley P, Friedman L, Meltzer H, Hedera P, Friedland R, Klein S, Thompson L, Detterman D, Tkach J, Lewin JS. 2D and 3D high resolution gradient echo functional imaging of the brain: venous contributions to signal in motor cortex studies. *NMR Biomed* 1994;7:54–62.
- Cho ZH, Ro YM. Reduction of susceptibility artifact in gradient-echo imaging. *Magn Reson Med* 1992;23:193–200.
- Glover G, Lai S. Reduction of susceptibility effects in BOLD fMRI using tailored RF pulses. In: *Proceedings of the Sixth Annual Meeting of the ISMRM, Sydney, 1998*, p 298.
- Yang QX, Dardzinski BJ, Li S, Eslinger PJ, Smith MB. Multi-gradient echo with susceptibility inhomogeneity compensation (MGESIC): demonstration of fMRI in the olfactory cortex at 3.0 T. *Magn Reson Med* 1997;37:331–335.
- Constable R, Spencer D. Composite image formation in Z-shimmed functional MR imaging. *Magn Reson Med* 1999;42:110–117.
- Irrazabal P, Nishimura DG. Fast three dimensional magnetic resonance imaging. *Magn Reson Med* 1995;33:656–662.
- Yang Y, Glover GH, van Gelderen P, Mattay VS, Santha AK, Sexton RH, Ramsey NF, Moonen CT, Weinberger DR, Frank JA, Duyn JH. Fast 3D functional magnetic resonance imaging at 1.5 T with spiral acquisition. *Magn Reson Med* 1996;36:620–626.
- Glover G. Basic and advanced concepts of spiral imaging. In: *ISMRM Fast MRI Workshop, 1997*, p 115–119.
- Pauly JM, Nishimura DG, Macovski A. A k-space analysis of small tip excitation. *J Magn Reson* 1989;81:43–56.
- Glover GH, Lai S. Self-navigated spiral fMRI: interleaved versus single-shot. *Magn Reson Med* 1998;39:361–368.
- Hayes C, Mathias C. Improved brain coil for fMRI and high resolution imaging. In: *ISMRM 4th Annual Meeting Proceedings, New York, 1996*, p 1414.
- Cohen MS. Parametric analysis of fMRI data using linear systems methods. *Neuroimage* 1997;6:93–103.
- Glover G. Deconvolution of impulse response in event-related BOLD fMRI. *Neuroimage* 1999;9:416–429.
- Bandettini PA, Jesmanowicz A, Wong EC, Hyde JS. Processing strategies for time-course data sets in functional MRI of the human brain. *Magn Reson Med* 1993;30:161–173.
- Lee AT, Glover GH. Discrimination of large venous vessels in time-course spiral blood oxygen dependent magnetic resonance functional neuroimaging. *Magn Reson Med* 1995;33:745–754.
- Worsley KJ, Friston KJ. Analysis of fMRI time-series revisited—again [comment]. *Neuroimage* 1995;2:173–181.
- Kleinschmidt A, Requardt M, Merboldt K, Frahm J. On the use of temporal correlation coefficients for magnetic resonance mapping of functional brain activation. Individualized thresholds and spatial response delineation. *Int J Imaging Syst Technol*. 1995;6:238–244.
- King KF. Spiral scanning with anisotropic field of view. *Magn Reson Med* 1998;39:448–456.